High-temperature, spectrally-selective, scalable, and flexible thin-film Si absorber and emitter

ZHIGUANG ZHOU,[1] HAO TIAN,[1] THOMAS M. HYMEL,[2] HARSHA REDDY,[1] VLADIMIR M. SHALAEV,[1] YI CUI,[2] AND PETER BERMEL[1,*]

[1]*Birck Nanotechnology Center, Purdue University, 1205 West State St., West Lafayette, Indiana 47907, USA*
[2]*Material Science and Engineering, Stanford University, McCullough Building, 476 Lomita Mall, Stanford, California 94305, USA*
*pbermel@purdue.edu

Abstract: Solar thermal technologies have great potential to provide low-cost storage for solar energy. However, their efficiencies are limited by a lack of scalable, mechanically flexible, durable, yet highly-efficient spectrally-selective solar absorbers suitable for high temperatures at low solar concentrations. Here, we overcome these challenges by fabricating a scalable free-standing spectrally-selective thin-film Si absorber and emitter (SSTFS) composite. Its high-temperature emittance shows strong spectral selectivity, even at 595 °C. Thermal stability is proven by measuring optical properties before and after thermal cycling equivalent to one day of concentrated sunlight. Despite the use of crystalline Si, the fabricated SSTFS composite exhibits exceptional mechanical flexibility to cover most surface geometries. The SSTFS composite demonstrates the potential of high-temperature, efficient and flexible solar absorbers and thermal emitters to advance renewable solar energy with storage.

1. Introduction

Solar thermal technologies provide a promising complement to solar photovoltaics. Since they first capture sunlight as heat, and then convert it to electricity, they can readily incorporate low-cost storage for power generation at night. The efficiency of the first step depends on the specific application, but is limited by the optical properties of the solar absorber at high temperatures. These particularly include the solar absorptance of the absorber and its losses from thermal re-radiation. Both factors relate directly to the absorptance spectrum of the solar absorber over a broad spectral range. The thermal transfer efficiency η_t captures the trade-off between these two factors [1]. For a given solar concentration C and operating temperature T, η_t is given by:

$$\eta_t = \bar{\alpha} - \frac{\bar{\varepsilon}\sigma T^4}{CI}, \tag{1}$$

where I is the solar irradiance (1 kW/m² is the solar constant); and $\bar{\alpha}$ and $\bar{\varepsilon}$ are the spectrally-averaged solar absorptance and thermal emittance, respectively. Both can be calculated from the absorptance spectrum of the absorber [1,2]. Based on this formula, having only a high $\bar{\alpha}$ does not guarantee a high η_t. In fact, a spectrally-selective absorber is needed, with absorptance in the wavelength range 0.3–2.0 µm close to unity, and emittance at longer wavelengths close to zero. High spectral selectivity is particularly critical for high operating temperatures and low solar concentrations, conditions that attract much attention due to the combination of higher Carnot efficiency and lower (or zero) cost for solar tracking. Prior work demonstrated that such spectral selectivity can be achieved by composite materials like cermets [3–5], where metallic nanoparticles are embedded in ceramic binders. Furthermore, multilayer structures [6], photonic crystals [7–10] and plasmonic structures [11–13] can tailor the absorptance and emittance spectrum of bulk materials [14,15], thereby giving rise to strong spectral selectivity. Recent

reviews have shown that there are often significant trade-offs between performance, durability, and costs [1,2].

To convert high-temperature solar heat into electricity, thermophotovoltaic (TPV) systems stand out among various technologies [16,17] due to high theoretical maximum efficiencies [18] as well as high power densities [19]. The value of thermophotovoltaics (TPV) also extends well beyond solar energy. It has also been proposed for applications such as recovering waste heat [2,20] and power generation from fuels [19]. The energy conversion process in TPV consists of two steps. First, a thermal emitter converts heat into thermal radiation. Second, a photovoltaic (PV) diode converts the incident radiation into electricity [2]. A good thermal emitter should have high emittance only over a certain bandwidth above the bandgap energy of the PV diode, and near-zero emittance elsewhere [9].

Complex nanophotonic structures similar to spectrally-selective absorbers may serve as highly selective emitters, since Kirchhoff's law of thermal radiation [21] predicts absorptivity equals emissivity at every wavelength in thermal equilibrium. For example, metamaterials have been demonstrated in prior work to serve as highly selective emitters [22,23]. It is also crucial that the spectral selectivity holds even at elevated temperatures. In prior work, photonic crystal emitters on refractory metals (similar to photonic crystal absorbers) have been proposed [24] and demonstrated [25]. Plasmonic structures based on refractory materials like titanium nitride have also demonstrated significant spectral selectivity and excellent thermal stability [26].

While prior literature has primarily focused on measures such as thermal transfer efficiency, there are in fact three critical figures of merit for selective solar absorber materials relevant to real applications: scalable manufacturing, mechanical flexibility, and good high-temperature performance. Absorber/emitters that meet all three criteria have yet to be reported in the literature. Those with excellent spectral selectivity, such as nanophotonic structures, are difficult to scale up because of both fabrication methods and raw material costs. Their rigid substrates also limit mechanical flexibility, causing difficulties when applied to non-flat surfaces. Low-cost cermets are commercially available as an alternative, but have limited maximum temperatures and lifetimes. Extensive studies show that new, more expensive manufacturing techniques are required to realize improved performance [4].

To achieve a good balance of all three aforementioned figures of merit, we focus on improving a less-studied category known as the semiconductor-metal-dielectric trio. These composites can be as simple as a three-layer stack of anti-reflection coating (ARC), semiconductor absorber layer and metallic back reflector [1]. Low-cost, high-quality, earth-abundant semiconductor wafers are already commercially available from the microelectronics and photovoltaics industries. Semiconductor-metal tandems using silicon (Si) and germanium (Ge) have been theoretically proposed to be excellent selective solar absorbers [2,27]. Furthermore, thick single-crystal Si absorbers with surface texturing [28] and Si_3N_4 ARC [29] have been experimentally demonstrated. However, the thick Si layer greatly limits the mechanical flexibility and resilience. Furthermore, high-temperature characterization measurements show that thermal emittance due to intrinsic carrier concentration can increase rapidly with temperature [29], limiting the commercial relevance of thick Si absorbers for high-temperature applications (typically up to 550 °C). The performance of a thick Si wafer-based design in terms of all three figures of merit is therefore not sufficient for widespread use.

An effective way to suppress the effect of intrinsic carrier absorption is reducing the thickness of the semiconductor [29]. For instance, absorbers with reduced Si thickness have been fabricated by physical (PVD) or chemical vapor deposition (CVD) [30]; however, free-standing, single-crystal Si thin-films have not been used for such applications. Their theoretical advantages of low mid-IR emittance, good thermal stability and strong mechanical flexibility are outstanding. But fabricating single-crystal thin-film Si using conventional growth methods imposes significant challenges [31–33]. Fortunately, it has recently been demonstrated that direct wet etching of

a commercial single-crystal wafer can provide free-standing thin-films of high quality [34]. Following an improved, CMOS-compatible procedure, a free-standing single-crystal spectrally-selective thin-film Si absorber/emitter (SSTFS) composite material is fabricated here. Instead of performing nano-texturing as demonstrated in [34], a substantially different fabrication method is taken. Here, an anti-reflection coating and back reflector are both added for this free-standing thin-film. It is a simple three-layer structure consisting only of commercially available materials, required for scalability. Its structure excludes any rigid substrate, allowing strong mechanical flexibility. Furthermore, high spectral selectivity has been experimentally proved in this work, matching closely with theory. The SSTFS is also proven to have good thermal stability, capable of withstanding high operating temperatures for many hours at a time. Our work shows that with optimization, SSTFS composites can have a good balance of scalable manufacturing, mechanical flexibility and good high-temperature spectral selectivity and durability.

2.   Fabrication and high-temperature characterization

The SSTFS studied in this work preserves some of the best features of the spectrally-selective wafer-based Si (SSWS) investigated in prior work [29]. There is generally a trade-off between suppressing emission ($\bar{\varepsilon}$) and maintaining absorption ($\bar{\alpha}$), which varies with thickness. As a result, the optimal thickness of Si is around 10 μm [29].

2.1.   Fabrication

The fabrication of SSTFS consists of three steps: (1) etching commercial Si wafer to target thickness; (2) Deposition of Ag back reflector; (3) Deposition of Si_3N_4 ARC. Starting from step (1), lightly doped (1–10 $\Omega \cdot$ cm) double-side-polished n-type (100) wafers are first masked with a PECVD-deposited 500 nm silicon nitride (SiN_x) layer around the edges, creating a thick handling ring for future ease of handling. The wafers are then loaded into a cassette and dipped into 2% hydrofluoric acid (HF) to etch the native oxide before the Si etching bath. After a DI water rinse, the wafer cassette is placed into a 25% tetramethylammonium hydroxide (TMAH) solution held at 90 °C for the duration of the etch. Once the wafers are etched to the desired thickness, they are removed from the TMAH etch bath, rinsed with DI water, and blown dry with nitrogen gas. For step (2), a 300 nm silver layer is deposited on the backside of the thin-film by e-beam evaporator (CHA) at a rate of 1.5 $Ås^{-1}$. Finally, in step (3), a 92 nm silicon nitride (Si_3N_4) ARC is sputtered at the front side using a magnetron sputtering system (custom-built by PVD Products) using a 100 W AC power supply and 5 mTorr with 15 sccm Ar (see Appendix C for the entire process flow).

The cross-section of the fabricated SSTFS is shown schematically in Fig. 1(a). The dimension of each layer is extracted by fitting the room-temperature emittance spectrum with numerical simulations. As shown in Fig. 1(d), the blue curve is the emittance spectrum of our non-transparent sample characterized by reflectance (diffuse + specular) measurement, following Kirchhoff's law (emittance = 1- reflectance), using a Perkin Elmer Lambda 950 spectrophotometer with an integrating sphere. The spectral range is 300–2500 nm with a resolution of 5 nm. The spot size of the incident beam is about 0.5 ×1.0 cm². The theoretical room-temperature emittance (orange curve) is simulated using S4 [35], and the materials are modelled as in Tian *et al*. [29].

Figure 1(b) shows the as-fabricated SSTFS. Much like a Si thin-film fabricated via KOH etching [34], it can be easily cleaved into smaller pieces to tile surfaces. As shown in Fig. 1(c), the free-standing SSTFS is quite mechanically flexible – for instance, it conforms to an acrylic rod with 1.27 cm diameter without breaking.

2.2.   High-temperature thermal emittance measurements

Since the optical properties of most selective absorbers/emitters are temperature dependent, high-temperature optical characterization is essential to the proper study of SSTFS. To cover the broad spectral range from visible to mid-IR, two characterization techniques are used. For wavelengths
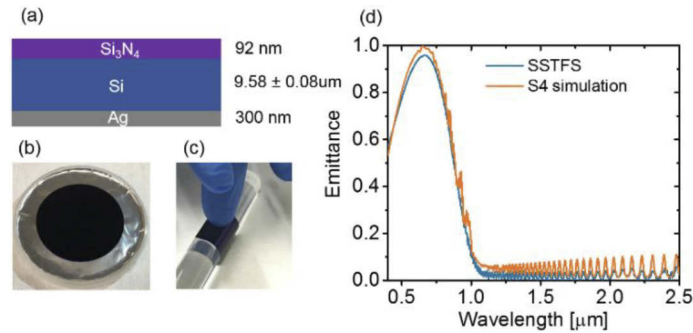
Fig. 1. (a) Cross-sectional schematic of the SSTFS. The thickness of Si_3N_4 and Si are determined by fitting the room-temperature emittance spectrum with a simulation in S4. (b) As-prepared SSTFS sample in a 10 cm wafer carrier. (c) The sample is mechanically flexible enough to wrap around a 1.27 cm diameter acrylic rod. (d) The measured room-temperature emittance spectrum matches simulations closely.

from 0.3 to 2.0 μm, the *in situ* high-temperature emittance is measured using a custom-built high-temperature ellipsometer [36,37] [see Fig. 2(a)]. To capture the high-temperature emittance from 2 to 10 μm, a custom-built direct thermal emittance measurement setup is used [29] [see Fig. 2(b)].
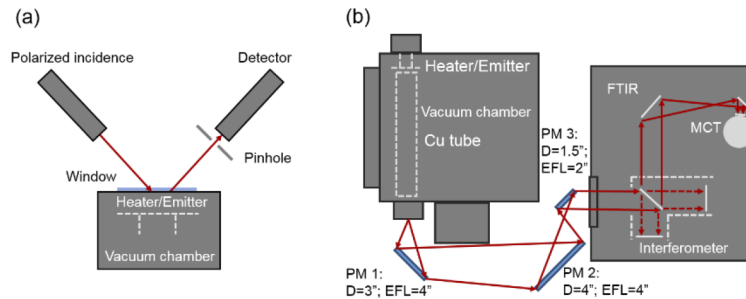

Fig. 2. High-temperature emittance characterization setup. (a) A customized high-temperature variable angle spectroscopic ellipsometer covering wavelengths from 0.3 to 2.0 μm. Samples are heated in a vacuum chamber. Temperature dependent specular reflectance spectra of s- and p-polarizations are measured through a quartz window at 18° angle of incidence. The pinhole blocks most of the background thermal radiation. (b) A custom-built direct thermal emittance measurement setup that covers wavelengths from 2 to 10 μm. The sample is heated in a high-vacuum chamber. The thermal emission signal is sent through optical elements, including an interior-polished copper tube and 3 off-axis parabolic mirrors (PM) with diameters (D) and effective focal lengths (EFL), to a Nexus 670 FTIR.

The experimental setup of the high-temperature ellipsometer is schematically illustrated in Fig. 2(a). The heating stage is integrated onto a variable angle spectroscopic ellipsometer (J.A. Woollam V-VASE UV-VIS-NIR). A quartz window on the vacuum (10^{-6} Torr) heating stage (Linkam TS1500V) provides optical access to the sample and a pinhole is placed in the reflected beam path to reduce the background thermal emission reaching the detector. Emittance is inferred as $1 - (R_s + R_p)/2$, where R_s and R_p are reflectance of s- and p-polarizations measured at an incident angle of 18°, respectively. The wavelength range of the high-temperature ellipsometry measurements is 0.3 - 2.0 μm with 10 nm wavelength steps. Calibration of this method is performed with a reference sample at room temperature. The presence of the window and the

pinhole introduces a scaling factor into the calibration. This scaling factor is first calibrated at room-temperature, as shown in Fig. 3, and is used to correct all subsequent high-temperature measurements. The high-temperature spectra are smoothed by a 5 adjacent point moving average to clearly depict the data.
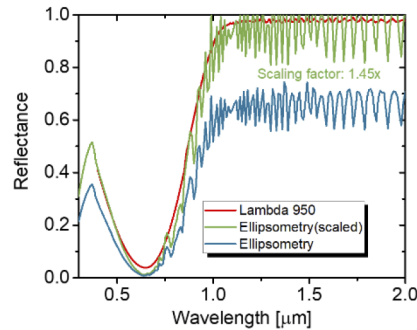

Fig. 3. Reflectance spectrum measurement using an ellipsometer, showing the procedure for calibrating the scaling factor. The ellipsometric spectrum measured with quartz window and pinhole installed (blue curve) is re-calibrated to the green curve, to match with the independent specular + diffuse reflectance (red curve) measurement by a Perkin Elmer Lambda 950 spectrophotometer (with an integrating sphere attachment). The scaling factor in this work of 1.45 provides a good match, such that reflectance does not exceed 100%.

The experimental setup of the direct thermal emittance measurement is schematically illustrated in Fig. 2(b). The heating stage (HTR1001, Tectra) used to heat the sample is installed in the vacuum chamber ($\sim 10^{-7}$ Torr) and is controlled by a PID controller. For good thermal contact with the heater, the thin-film samples are attached to graphite foil using high-temperature silver paste (597-A, Aremco). As shown in Fig. 2(b), the thermal emission signal is collected by the copper tube and collimated by 3 off-axis parabolic mirrors (PM 1, 2 and 3, Edmund Optics) to the Fourier-transform InfraRed Spectroscopy (FTIR, Thermo Fisher Scientific Nexus 670) that has a liquid nitrogen cooled (77 K) mercury cadmium telluride (MCT) detector. The interferometer has an XT-KBr beam splitter that extends the spectral range of detection. To measure such a broad band spectrum, a low mirror velocity of 0.1581 cm·s^{-1} is set. Each spectrum is averaged over 100 scans for acceptable signal to noise ratio. The high-temperature emittance measurements are calibrated by using a 1.1 cm × 1.1 cm vertically grown multi-wall carbon nanotube (MWCNT) as the reference ($\alpha = 0.95$ at room temperature). Temperature of the sample is directly measured by a type K thermocouple (SCASS-020U-12-SHX, Omega) attached by high-temperature silver paste (597-A, Aremco).

2.3.   *Simulation of high-temperature emittance*

The theoretical high-temperature emittance spectra in the range of 0.4 - 10 μm are simulated using S4 [35]. For high-temperature simulations, the complex refractive index of Si_3N_4 is extracted from the work by Kischkat *et al*. [38]. Temperature-dependent dielectric constant of Ag is calculated using the Drude-Lorentz parameters derived by Reddy *et al*. [37]. For Si, a semi-empirical model [39] is used to calculate high-temperature refractive index. To match different experimental conditions of the two measurement techniques, emittance simulations are performed at 18° in 0.4 - 2 μm (for ellipsometry setup), and angular-averaged from 0 to 32° in 2.0 - 10 μm (for direct thermal emittance measurement setup). The angular-averaged spectra in 2.0 - 10 μm are given by $\int_0^{\theta_0} d\theta \varepsilon(\lambda, \theta) \cos(\theta) \sin(\theta) / \int_0^{\theta_0} d\theta \cos(\theta) \sin(\theta)$, where $\epsilon(\lambda, \theta)$ is the emittance at wavelength λ and angle θ; $\theta_0 = 32°$. In Fig. 4(a) - (b), both spectra are separated into two regions (shaded red and unshaded), reflecting different characterization techniques.
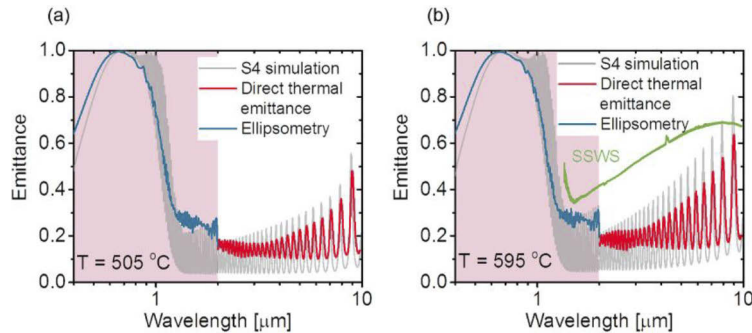
Fig. 4. High-temperature T emittance spectra for SSTFS: (a) $T = 505$ °C, (b) $T = 595$ °C. The high-temperature ellipsometry data (blue curves) and direct thermal emittance measurement data (red curves) are plotted together with numerical simulation results (gray curves) for comparison. Overall, a good match is observed. The high-temperature emittance of an SSWS measured at 535 °C [29] is also plotted in (b) (green curve). The reduced Si thickness suppresses $\bar{\varepsilon}$ from 0.60 to 0.23, even though the temperature is 60 °C higher.

3. Results

The high-temperature emittance spectra measured at two temperatures using the aforementioned techniques are plotted in Fig. 4(a) - (b). High-temperature simulations are shown for comparison (gray curves). As discussed in Section 2.3, the differences between the two characterization techniques affects our interpretation, giving rise to a jump as we transition between the two techniques at 2.0 μm. For both temperatures (505 °C and 595 °C), the experimental data matches well with our simulations. An increase in the mid-IR emittance is observed as temperature rises, induced by higher intrinsic carrier concentrations. In Fig. 4(b), the emittance spectrum of an SSWS measured at 535 °C [29] is plotted (green curve) for comparison. Significant suppression of mid-IR emittance is achieved, which would lead to less re-radiation loss for solar thermal applications and less sub-bandgap emission loss in TPV applications, compared to its wafer-based counterpart.

For solar thermal applications, the measured emittance of SSTFS gives $\bar{\alpha} = 0.76$ and $\bar{\varepsilon} = 0.23$ at 595 °C. The thermal transfer efficiency η_t, following Eq. (1), is 0.61 under 50 suns. However, the SSWS, even at a lower temperature (535 °C), has $\bar{\varepsilon} = 0.60$ over the spectral range of the green curve in Fig. 4(b). As expected, the reduced Si thickness strongly suppresses thermal re-radiation. Compared with other state-of-the-art selective absorbers reviewed in [4], the SSTFS shows strong suppression of thermal emittance at the operating temperature. Since emittance increases with temperature, this compares favorably with values summarized in [4], which were mostly measured at low temperature or extrapolated from room temperature. Furthermore, although the solar absorptance of SSTFS is slightly lower than those listed in [4], a near 15% relative improvement can be achieved without sacrificing the structural simplicity using a multi-layer ARC [2]. Importantly, all of the absorbers listed in [4] have substrates, which limit their mechanical flexibility. In contrast, the SSTFS demonstrated in our work is a free-standing thin-film that can conformally cover curved surfaces. Such unique property, combined with its good optical performance at high-temperature, makes our SSTFS more adaptable to real applications.

The SSTFS also shows major advantages as a selective thermal emitter for TPV applications. First, its strong spectral selectivity at high temperatures is desirable for high system efficiencies. One way to quantify this is calculating the spectral averaged emittance for above-bandgap

spectrum $\bar{\varepsilon}_{above}$ and below-bandgap spectrum $\bar{\varepsilon}_{below}$ as:

$$\bar{\varepsilon}_{above} = \int_{0.3}^{\lambda_g} d\lambda \varepsilon(\lambda) BB(\lambda, T) / \int_{0.3}^{\lambda_g} d\lambda BB(\lambda, T), \tag{2}$$

$$\bar{\varepsilon}_{below} = \int_{\lambda_g}^{10} d\lambda \varepsilon(\lambda) BB(\lambda, T) / \int_{\lambda_g}^{10} d\lambda BB(\lambda, T), \tag{3}$$

where λ_g is the wavelength [μm] corresponding to the bandgap of PV diode; $BB(\lambda, T)$ is the Planck's blackbody radiation function at wavelength λ [μm] and temperature T. Assuming a TPV system with the bandgap of PV diode at 1.1 eV, such as c-Si PV, the above-bandgap spectrally-average emittance $\bar{\varepsilon}_{above} = 0.68$, while the sub-bandgap spectrally-average emittance $\bar{\varepsilon}_{below} = 0.23$ at 595 °C. Second, low sub-bandgap emittance may reduce PV diode heating, helping to maintain high TPV efficiencies [40]. In real TPV applications, the two factors discussed above depend not only on the thermal emitter, but also on the PV diode and other system parameters. Therefore, a system-level comparison must be performed.

4. Discussion

The improvement in spectral selectivity, as demonstrated above, can greatly enhance the performance of semiconductor-metal-dielectric trio in high-temperature applications. To illustrate such enhancement, we compare the performance of an SSTFS with an SSWS [29] in solar thermal and TPV applications. The strong agreement between measured high-temperature emittance and theory indicates our model may be safely interpolated to intermediate temperatures where characterization has not yet been performed. For fair comparison, the thickness of Si_3N_4 in both structures is set to 92 nm, consistent with the fabricated SSTFS. Per Tian *et al.* [29], such thickness of Si_3N_4 is very close to its optimal value.

4.1. Selective solar absorber

Figure 5 shows the $\bar{\alpha}$ (orange curves), $\bar{\varepsilon}$ (blue curves) and η_t (green curves) of the SSTFS (triangle symbol) and SSWS (square symbol) as solar absorbers at various temperatures and 50 sun concentration. $\bar{\alpha}$ of the SSTFS is always slightly lower than the SSWS, since Si has an indirect bandgap. However, the $\bar{\varepsilon}$ of the SSWS increases rapidly with temperature, while the $\bar{\varepsilon}$ of the SSTFS remains low. As a result, the η_t of SSTFS is higher once the temperature passes 450 °C. The improvement in η_t is most pronounced at higher temperatures, corresponding to a 52% relative increase around 600 °C.
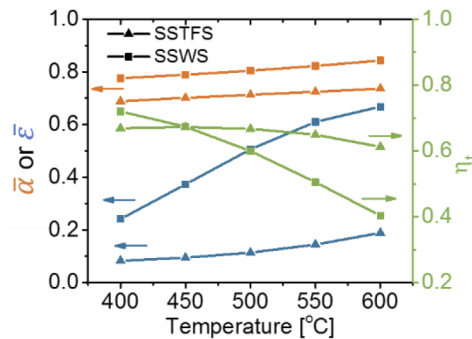

Fig. 5. Selective solar absorbers. The $\bar{\alpha}$ (orange curves) and $\bar{\varepsilon}$ (blue curves) are simulated at different operating temperatures for SSTFS (triangle symbol) and SSWS (square symbol), respectively. The thermal transfer efficiencies (green curves) are calculated assuming 50 sun concentration. SSTFS outperform SSWS at temperatures > 450 °C.

4.2. Selective TPV emitter

Another important application is the selective emitter for a TPV system. As mentioned above, reduced spectral selectivity of emitters not only increases losses from sub-bandgap emission, but also decreases PV diode efficiencies through heating. Both factors significantly impact the conversion efficiency. Figure 6 compares the efficiencies of two TPV systems with different selective emitters: an SSTFS and an SSWS. The relative increase in TPV efficiency, given by $RI_{tpv} = (\eta_{tpv-t} - \eta_{tpv-w})/\eta_{tpv-w}$, is calculated for various PV bandgaps and emitter temperatures, where η_{tpv-t} and η_{tpv-w} are the TPV efficiencies for SSTFS and SSWS, respectively. The TPV performance is estimated at various emitter temperatures (400 - 600 °C) and PV bandgaps (0.5–1.2 eV). For PV diodes at different bandgaps, an external quantum efficiency (EQE) of 0.9 and ideality factor of 1 are assumed. Dark current density at room temperature is calculated by a realistic model that reflects the state-of-the-art PV performances [41]. The view factor F from emitter to PV diode is assumed to be 0.99.
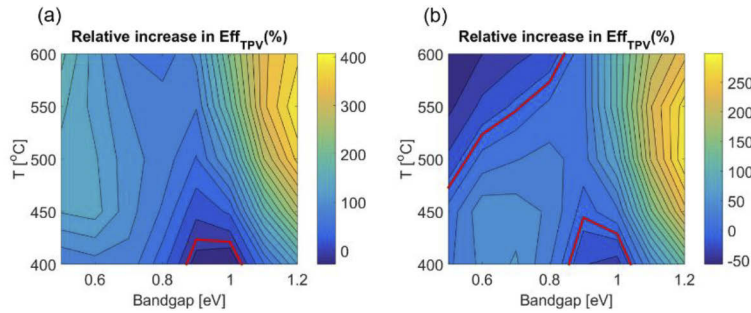

Fig. 6. Selective TPV emitters. The relative increase of TPV efficiency (RI_{tpv}) when the SSWS is replaced by the SSTFS, is calculated for different PV bandgaps and emitter temperatures. (a) Parasitic heating of PV diode is considered. (b) The PV diode temperature is assumed to be 300 K. Except for the area enclosed by the red curve, where RI_{tpv} is negative, reduced sub-bandgap emission and PV diode heating significantly improves TPV efficiencies.

For Fig. 6(a), a more realistic TPV model is used, which incorporates PV diode heating from unused radiation in a self-consistent manner. The temperature of PV diode is determined by solving the power balance equation: $FP_{emit} = P_{ele}(T_{PV}) + P_{dis}(T_{PV}) + P_{rad}(T_{PV})$, where P_{emit} is the total emitted power from the emitter; $P_{ele}(T_{PV})$ is the electrical power output from PV diodes at temperature T_{PV}; $P_{dis}(T_{PV})$ and $P_{rad}(T_{PV})$ are the heat dissipation of PV diodes through non-radiative heat transfer and radiative heat transfer, respectively. An effective cooling coefficient of 20 mW·K^{-1} is assumed so that the maximum PV temperature is below 200 °C. The PV diodes are assumed to have 100% absorption across the spectral range considered to take into account the fact that most PV diodes have sub-bandgap absorption.

Figure 6(a) indicates that the SSTFS is superior to the SSWS for most PV bandgaps and emitter temperatures considered, except for the area below the red curve, where RI_{tpv} is negative. Although the absolute TPV efficiency is limited by the operating temperature, the relative increase in efficiency is significant, especially for high emitter temperatures and large bandgap PV diodes (> 1 eV). For example, when a c-Si PV diode with bandgap of 1.1 eV is used and the emitter is at a temperature of 600 °C, RI_{tpv} is as high as 340%. This can be explained by the fact that SSTFSs are more selective than SSWSs at elevated temperatures, suppressing *both* the sub-bandgap emission loss and parasitic heating of the PV diode. Even when the PV diode temperature is well-controlled at 300 K, as shown in Fig. 6(b), RI_{tpv} can still reach 200%.

5.   Thermal stability

In practical solar thermal and TPV applications, the absorber and the emitter must withstand high-temperature operation at least several hours a day. Typically, the highest concentrations of sunlight are available around 6 hours (hr) per day under clear skies [42]. Therefore, it is important to investigate the thermal stability of SSTFS structures in such time scales. In this work, an SSTFS sample is heated to 600 °C under ultra-high vacuum ($\sim 10^{-7}$ Torr) for two thermal cycles. The first cycle (thermal cycle #1) dwells at the maximum temperature for 1 hr; the second (thermal cycle #2), for 5 hr more (see Appendix A). After each thermal cycle, a room-temperature emittance spectrum is measured. Figure 7 compares the emittance before and after each thermal cycle. The interference fringe amplitude is smaller than the high-temperature results, due to much weaker absorption in Si and the larger size of the incident beam used in room-temperature reflectance measurements. A slight degradation in IR reflection occurs after thermal cycle #1, while the emittance peak stays nearly intact. After thermal cycle #2, the degradation slows down significantly even with a 5x longer dwell time. The overall spectral selectivity is maintained after 6 hr total annealing. Room-temperature emittance spectra and Scanning Electron Microscope (SEM) images after a much longer operation time (24 hr thermal cycle, see Appendix B) reveals partial delamination. Given that most of the degradation happens at energies below the Si bandgap, and that the thin-film Si is stable even at 900 °C for 4 hr, we conclude that the dominant mechanism is the degradation of the Ag back reflector and/or the Si/Ag interface. Therefore, further improvement in thermal stability lies in replacing Ag with a refractory back reflector. Nonetheless, the SSTFS shows great thermal stability at 600 °C over a 6 hr period of time, closely resembling a real (outdoor) application.
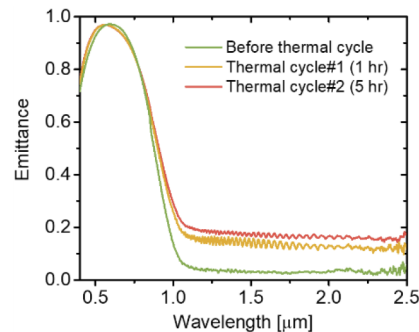

Fig. 7. Thermal stability test. Room-temperature emittance spectra of SSTFS are measured before thermal cycle (green curve), after the first thermal cycle that dwells at 600 °C for 1 hr (yellow curve) and after the second thermal cycle that dwells at 600 °C for 5 hr (red curve). Slight elevation in emittance is observed and is mainly caused by the degradation of the Ag back reflector.

6.   Conclusions

In summary, we have fabricated a free-standing, high temperature, spectrally-selective thin-film Si absorber/emitter (SSTFS) composite that exhibits a good balance of all three figure of merits for new solar thermal or TPV applications. Its standardized CMOS-compatible fabrication processes make it possible for scalable manufacturing. Its tremendous mechanical flexibility allows it to be adapted to a wide range of applications. High-temperature emittance characterization has been performed, and shows an excellent match with the corresponding numerical simulations. Compared with its wafer-based counterpart, the thin-film design strongly suppresses thermal emittance in the mid-IR, resulting in a stronger spectral selectivity and superior performance

across a broad range of operating conditions for solar thermal and TPV. Furthermore, its thermal stability is demonstrated in multiple long-term thermal cycles, corresponding to prospective use cases. The presented selective absorber/emitter design strategy is certainly not restricted to Si, Ag and Si_3N_4. Further improvements are possible for SSTFS composites. For example, a multi-layer ARC may improve the solar absorptance. Direct-bandgap semiconductors may replace Si and effectively suppress free-carrier absorption without sacrificing above-bandgap absorption. Also, thermal stability / lifetime may be further enhanced by replacing Ag with refractory metals in future work. Other thin-film fabrication technologies, such as anisotropic wet etching of a Si boule, epitaxial lift-off, or high-throughput techniques like solution processing/ roll-to-roll printing, may further reduce the combined material and fabrication costs. Most importantly, this work paves the way for large-scale development and deployment of efficient, low-cost, and flexible selective solar thermal absorbers/emitters, which might be particularly beneficial for producing high-temperature steam in low concentrating selective absorbers, as well as opening up new possibilities for future solar and thermal technologies.

Appendix A: temperature profiles of thermal cycles

The temperature profile utilized in the thermal cycling associated with this work is provided in Fig. 8.
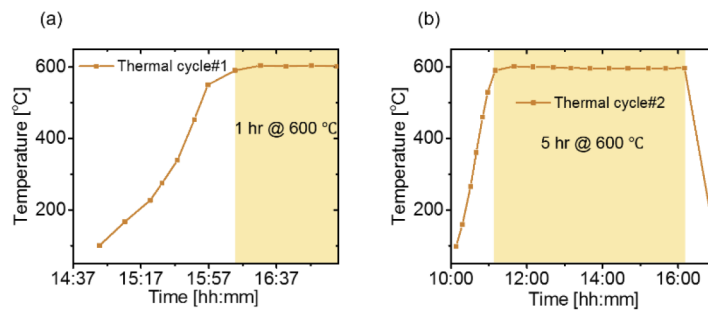

Fig. 8. Full temperature profiles of the two thermal cycles used for the thermal stability tests. a) The first cycle (thermal cycle #1) dwells at 600 °C for 1 hr and b) the second cycle (thermal cycle #2) dwells at 600 °C for 5 hr. Both cycles are performed on the same sample under ultra-high vacuum (~ 10^{-7} Torr). The temperature is measured by a type K thermocouple attached to the sample by silver paste (597-A, Aremco). The same sample remains at 600 °C for 6 hr in total.

Appendix B: 24-hr thermal cycle

To test the lifetime of the SSTFS, 4 consecutive 6-hr thermal cycles are performed on a pristine sample. Maximum temperature for each thermal cycle is still 600 °C. Room temperature emittance spectra are measured at various spots on the sample surface after the fourth thermal cycle. As shown in Fig. 9, more significant degradation is observed.

It should be noted as well that the extent of degradation varies with the location, indicating non-uniform delamination in the structure. To further explore the root cause, Scanning Electron Microscope (SEM) images are taken from the back side of the SSTFS. As shown in Fig. 10, discontinuity in the Ag layer is apparent. As we zoom in the view [Fig. 10(a)-(d)], traces of Ag dewetting the Si surface, a well-known effect [37], can be found.
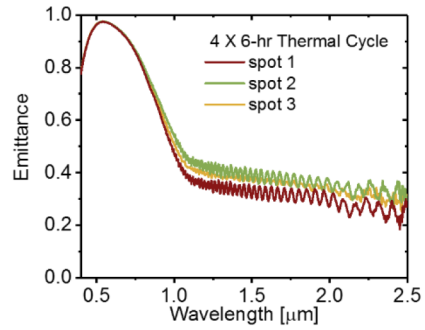
Fig. 9. 24 hr Thermal stability test. Room-temperature emittance spectra of SSTFS are measured the 4th 6-hr thermal cycle that dwells at 600 °C. More significant elevation in emittance is observed and the degradation varies with location.
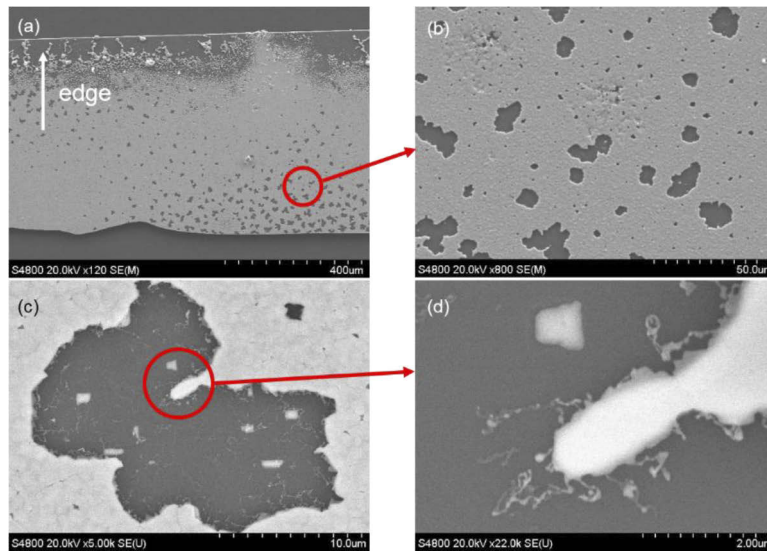

Fig. 10. SEM images of the back side of SSTFS after 24 hr Thermal stability test. (b) Corresponds to the circled area in (a). (c) same image, zoomed in further, and (d) corresponds to the circled area in (c). Apparent dewetting effect of Ag from Si surface is observed.

Appendix C: SSTFS fabrication process flow

The large-area free-standing SSTFS composite material is fabricated following the steps outlined in Fig. 11 above: creating a handling ring, performing oxide removal, wet etching, silver and silicon nitride deposition, laser cutting, and finally, removal of the SSTFS.
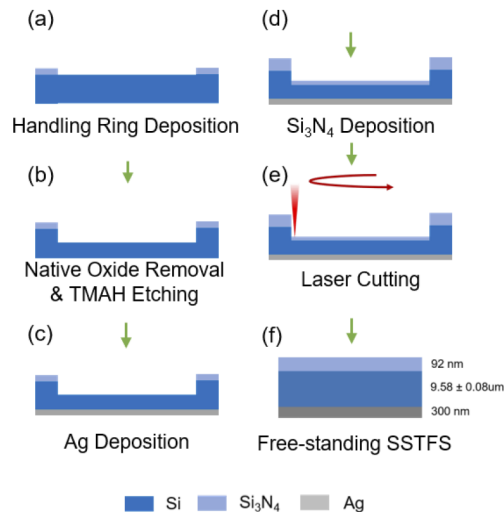

Fig. 11. Fabrication process flow of SSTFS. (a) SiN_x handling ring PECVD deposition. (b) Thin-film wafer fabricated by TMAH wet etching. (c) Ag back reflector deposition by e-beam evaporation. (d) Si_3N_4 deposition by sputtering. (e) Handling ring removal by laser cutting. (f) The fabricated free-standing SSTFS composite material.

Disclosures

The authors declare no conflicts of interest.

References

1. P. Bermel, J. Lee, J. D. Joannopoulos, I. Celanović, and M. Soljačić, "Selective solar absorbers," Annu. Rev. Heat Transfer **15**(15), 231–254 (2012).
2. P. Bermel, M. Ghebrebrhan, W. Chan, Y. X. Yeng, M. Araghchini, R. Hamam, C. H. Marton, K. F. Jensen, M. Soljačić, J. D. Joannopoulos, S. G. Johnson, and I. Celanović, "Design and global optimization of high-efficiency thermophotovoltaic systems," Opt. Express **18**(S3), A314–A334 (2010).
3. D. Chester, P. Bermel, J. D. Joannopoulos, M. Soljačić, and I. Celanović, "Design and global optimization of high-efficiency solar thermal systems with tungsten cermets," Opt. Express **19**(S3), A245–A257 (2011).
4. F. Cao, K. McEnaney, G. Chen, and Z. Ren, "A review of cermet-based spectrally selective solar absorbers," Energy Environ. Sci. **7**(5), 1615–1627 (2014).
5. F. Cao, D. Kraemer, T. Sun, Y. Lan, G. Chen, and Z. Ren, "Enhanced thermal stability of W-Ni-Al2O3Cermet-based spectrally selective solar absorbers with tungsten infrared reflectors," Adv. Energy Mater. **5**(2), 1401042 (2015).

6. H. Wang, H. Alshehri, H. Su, and L. Wang, "Design, fabrication and optical characterizations of large-area lithography-free ultrathin multilayer selective solar coatings with excellent thermal stability in air," Sol. Energy Mater. Sol. Cells **174**, 445–452 (2018).

7. I. Celanović, N. Jovanovic, and J. Kassakian, "Two-dimensional tungsten photonic crystals as selective thermal emitters," Appl. Phys. Lett. **92**(19), 193101 (2008).

8. V. Rinnerbauer, E. Lausecker, F. Schäffler, P. Reininger, G. Strasser, R. D. Geil, J. D. Joannopoulos, M. Soljačić, and I. Celanović, "Nanoimprinted superlattice metallic photonic crystal as ultraselective solar absorber," Optica **2**(8), 743–746 (2015).

9. E. Rephaeli and S. Fan, "Absorber and emitter for solar thermo-photovoltaic systems to achieve efficiency exceeding the Shockley-Queisser limit," Opt. Express **17**(17), 15145–15159 (2009).

10. P. Li, B. Liu, Y. Ni, K. K. Liew, J. Sze, S. Chen, and S. Shen, "Large-Scale Nanophotonic Solar Selective Absorbers for High-Efficiency Solar Thermal Energy Conversion," Adv. Mater. **27**(31), 4585–4591 (2015).

11. D. Woolf, J. Hensley, J. G. Cederberg, D. T. Bethke, A. D. Grine, and E. A. Shaner, "Heterogeneous metasurface for high temperature selective emission," Appl. Phys. Lett. **105**(8), 081110 (2014).

12. M. R. Khan, X. Wang, E. Sakr, M. A. Alam, and P. Bermel, "Enhanced selective thermal emission with a meta-mirror following Generalized Snell's Law," Mater. Res. Soc. Symp. Proc. **1728**, 0–5 (2015).

13. H. Wang, V. Prasad Sivan, A. Mitchell, G. Rosengarten, P. Phelan, and L. Wang, "Highly efficient selective metamaterial absorber for high-temperature solar thermal energy harvesting," Sol. Energy Mater. Sol. Cells **137**, 235–242 (2015).

14. M. Ghebrebrhan, P. Bermel, Y. X. Yeng, I. Celanović, M. Soljačić, and J. D. Joannopoulos, "Tailoring thermal emission via Q matching of photonic crystal resonances," Phys. Rev. A **83**(3), 033810 (2011).

15. Y. X. Yeng, M. Ghebrebrhan, P. Bermel, W. R. Chan, J. D. Joannopoulos, M. Soljačić, and I. Celanović, "Enabling high-temperature nanophotonics for energy applications," Proc. Natl. Acad. Sci. **109**(7), 2280–2285 (2012).

16. D. M. Bierman, A. Lenert, W. R. Chan, B. Bhatia, I. Celanović, M. Soljačić, and E. N. Wang, "Enhanced photovoltaic energy conversion using thermally based spectral shaping," Nat. Energy **1**(6), 16068 (2016).

17. D. Kraemer, B. Poudel, H. Feng, J. C. Caylor, B. Yu, X. Yan, Y. Ma, X. Wang, D. Wang, A. Muto, K. McEnaney, M. Chiesa, Z. Ren, and G. Chen, "High-performance flat-panel solar thermoelectric generators with high thermal concentration," Nat. Mater. **10**(7), 532–538 (2011).

18. A. Datas and A. Martí, "Thermophotovoltaic energy in space applications: Review and future potential," Sol. Energy Mater. Sol. Cells **161**, 285–296 (2017).

19. W. R. Chan, P. Bermel, R. C. N. Pilawa-Podgurski, C. H. Marton, K. F. Jensen, J. J. Senkevich, J. D. Joannopoulos, M. Soljačić, and I. Celanović, "Toward high-energy-density, high-efficiency, and moderate-temperature chip-scale thermophotovoltaics," Proc. Natl. Acad. Sci. U. S. A. **110**(14), 5309–5314 (2013).

20. B. Bitnar, W. Durisch, and R. Holzner, "Thermophotovoltaics on the move to applications," Appl. Energy **105**, 430–438 (2013).

21. F. P. Incropera and D. P. DeWitt, *Fundamentals of Heat and Mass Transfer*, 5th ed. (John Wiley and Sons, 2002).

22. C. Wu, B. Neuner III, J. John, A. Milder, B. Zollars, S. Savoy, and G. Shvets, "Metamaterial-based integrated plasmonic absorber/emitter for solar thermo-photovoltaic systems," J. Opt. **14**(2), 024005 (2012).

23. P. N. Dyachenko, S. Molesky, A. Y. Petrov, M. Stormer, T. Krekeler, S. Lang, M. Ritter, Z. Jacob, and M. Eich, "Controlling thermal emission with refractory epsilon-near-zero metamaterials via topological transitions," Nat. Commun. **7**(1), 11809 (2016).

24. Z. Zhou, E. Sakr, O. Yehia, A. Mathur, and P. Bermel, "Photonic crystal selective structures for solar thermophoto-voltaics," MRS Adv. **1**(59), 3883–3889 (2016).

25. V. Rinnerbauer, A. Lenert, D. M. Bierman, Y. X. Yeng, W. R. Chan, R. D. Geil, J. J. Senkevich, J. D. Joannopoulos, E. N. Wang, M. Soljačić, and I. Celanović, "Metallic photonic crystal absorber-emitter for efficient spectral control in high-temperature solar thermophotovoltaics," Adv. Energy Mater. **4**(12), 1400334 (2014).

26. W. Li, U. Guler, N. Kinsey, G. V. Naik, A. Boltasseva, J. Guan, V. M. Shalaev, and A. V. Kildishev, "Refractory plasmonics with titanium nitride: Broadband metamaterial absorber," Adv. Mater. **26**(47), 7959–7965 (2014).

27. A. Donnadieu and B. O. Seraphin, "Optical performance of absorber-reflector combinations for photothermal solar energy conversion," J. Opt. Soc. Am. **68**(3), 292–297 (1978).

28. J. I. Gittleman, E. K. Sichel, H. W. Lehmann, and R. Widmer, "Textured silicon: A selective absorber for solar thermal conversion," Appl. Phys. Lett. **35**(10), 742–744 (1979).

29. H. Tian, Z. Zhou, T. Liu, C. Karina, U. Guler, V. M. Shalaev, and P. Bermel, "High temperature efficient, stable Si wafer-based selective solar absorbers," Appl. Phys. Lett. **110**(14), 141101 (2017).

30. B. O. Seraphin, "Chemical vapor deposition of thin semiconductor films for solar energy conversion," Thin Solid Films **39**, 87–94 (1976).

31. J. Poortmans and V. Arkhipov, eds., *Thin Film Solar Cells: Fabrication, Characterization and Applications* (John Wiley & Sons, Ltd, 2006).

32. J. C. Sturm and K. H. Chung, "Chemical Vapor Deposition Epitaxy of Silicon-based Materials using Neopentasilane," ECS Trans. **16**(10), 799–805 (2008).

33. D. L. Chubb, D. S. Wolford, A. Meulenberg, and R. S. DiMatteo, "Semiconductor silicon as a selective emitter," AIP Conf. Proc. **653**(1), 174–200 (2003).

34. S. Wang, D. W. Benjamin, Y. Li, K. X. Wang, E. Garnett, S. Fan, and Y. Cui, "Large-area free-standing ultrathin single-crystal silicon as processable materials," Nano Lett. **13**(9), 4393–4398 (2013).

35. V. Liu and S. Fan, "S4 : A free electromagnetic solver for layered periodic structures," Comput. Phys. Commun. **183**(10), 2233–2244 (2012).

36. H. Reddy, U. Guler, A. V. Kildishev, A. Boltasseva, and V. M. Shalaev, "Temperature-dependent optical properties of gold thin films," Opt. Mater. Express **6**(9), 2776–2802 (2016).

37. H. Reddy, U. Guler, K. Chaudhuri, A. Dutta, A. V. Kildishev, V. M. Shalaev, and A. Boltasseva, "Temperature-dependent optical properties of single crystalline and polycrystalline silver thin films," ACS Photonics **4**(5), 1083–1091 (2017).

38. J. Kischkat, S. Peters, B. Gruska, M. Semtsiv, M. Chashnikova, M. Klinkmüller, O. Fedosenko, S. Machulik, A. Aleksandrova, G. Monastyrskyi, Y. Flores, and W. T. Masselink, "Mid-infrared optical properties of thin films of aluminum oxide, titanium dioxide, silicon dioxide, aluminum nitride, and silicon nitride," Appl. Opt. **51**(28), 6789–6798 (2012).

39. F. Roozeboom, *Advances in Rapid Thermal and Integrated Processing* (Springer Science & Business Media, 2013).

40. J. R. Wilcox, A. W. Haas, J. L. Gray, and R. J. Schwartz, "Estimating saturation current based on junction temperature and bandgap," AIP Conf. Proc. **1407**(1), 30–33 (2011).

41. P. Bermel, K. Yazawa, J. L. Gray, X. Xu, and A. Shakouri, "Hybrid strategies and technologies for full spectrum solar conversion," Energy Environ. Sci. **9**(9), 2776–2788 (2016).

42. H. L. Zhang, J. Baeyens, J. Degreve, and G. Caceres, "Concentrated solar power plants: Review and design methodology," Renewable Sustainable Energy Rev. **22**, 466–481 (2013).